PAPER • OPEN ACCESS

Ex situ investigation of boron, hydrogen, and oxygen distributions on W7-X divertor surfaces using picosecond-LIBS under vacuum

To cite this article: Huace Wu *et al* 2026 *Nucl. Fusion* **66** 076049

OPEN ACCESS
IOP Publishing | International Atomic Energy Agency Nuclear Fusion
Nucl. Fusion **66** (2026) 076049 (17pp) https://doi.org/10.1088/1741-4326/ae7e05

Ex situ investigation of boron, hydrogen, and oxygen distributions on W7-X divertor surfaces using picosecond-LIBS under vacuum

Huace Wu[1,2], Christoph Kawan[2,3], Erik Wüst[2], Sebastijan Brezinsek[2,3,*], Rui Ding[4,*], Rongxing Yi[2], Timo Dittmar[2], Marcin Rasinski[2], Gennady Sergienko[2] and the W7-X Team[a]

[1] Institute of Energy, Hefei Comprehensive National Science Center (Anhui Energy Laboratory), 230031 Hefei, China
[2] Institute of Fusion Energy and Nuclear Waste Management—Plasma Physics, Forschungszentrum Jülich, 52425 Jülich, Germany
[3] Faculty of Mathematics and Natural Sciences, Heinrich Heine University Düsseldorf, 40225 Düsseldorf, Germany
[4] Institute of Plasma Physics, Chinese Academy of Sciences, 230031 Hefei, China

E-mail: s.brezinsek@fz-juelich.de and rding@ipp.ac.cn

Received 26 February 2026, revised 29 May 2026
Accepted for publication 16 June 2026
Published 2 July 2026

Abstract

Quantitative, spatially resolved measurements of near-surface material composition on plasma-facing components (PFCs) are critical for interpreting plasma–wall interaction (PWI) driven impurity sources, assessing wall-conditioning performance, and providing model constraints for impurity migration and co-deposition in present-day magnetic confinement devices and future reactors. In this work, picosecond laser-induced breakdown spectroscopy (ps-LIBS) is applied to post-mortem graphite divertor tiles from the stellarator Wendelstein 7-X (W7-X) under device-relevant high vacuum ($\sim 10^{-7}$ mbar) to obtain poloidally resolved two-dimensional maps and depth profiles of carbon (C), boron (B), hydrogen (H), and oxygen (O). The ps-LIBS results are cross-validated against isotope-sensitive diagnostics (nuclear reaction analysis, NRA; laser ablation molecular isotopic spectroscopy, LAMIS) and complemented by profilometry, focused ion beam scanning electron microscopy (FIB-SEM)/energy-dispersive x-ray spectroscopy (EDS) and x-ray photoelectron spectroscopy (XPS) to relate lateral patterns to film thickness and near-surface chemistry. Pronounced poloidal heterogeneity is observed: the thickness of mixed co-deposited layers range from $\sim$0.3 to 0.4 μm in erosion-dominated regions, to $\sim$0.9 μm in B-rich deposition zones, and exceeds 12 μm in ^{13}C-rich deposits near the outer strike line after 2.5 h of H plasma operation. Depth profiling reveals that late-phase $^{13}CH_4$ injection forms a C–H–O enriched top layer that

* Authors to whom any correspondence should be addressed.
[a] See Grulke *et al* 2024 (https://doi.org/10.1088/1741-4326/ad2f4d) for the W7-X Team.

locally restructures the pre-existing boronized layer resulting from boronizations, including a pronounced subsurface B maximum at ∼4-5 μm. A calibration-based approach was established to estimate B/C ratios and B inventories from ps-LIBS, enabling quantitative evaluation across the B-rich region, the ^{13}C-rich deposition zone, and the erosion zone. The resulting poloidal and depth-resolved observables constitute benchmark-grade constraints for validating impurity transport/co-deposition modeling and support LIBS pathways toward in-vessel, near-real-time monitoring of surface elemental evolution under varying operational conditions.

Supplementary material for this article is available online

Keywords: boron, hydrogen, and oxygen distributions, picosecond-LIBS, W7-X divertor, Impurity migration and co-deposition, plasma–wall interaction

(Some figures may appear in colour only in the online journal)

1. Introduction

In magnetic confinement fusion, plasma–wall interaction (PWI) couples divertor and first-wall conditions to core-plasma purity, radiative losses and operational limits [1–3], while also controlling component lifetime and fuel retention through erosion, transport and deposition of impurities [4]. Wall-conditioning techniques such as boronization, lithiumization and siliconization are therefore employed to mitigate intrinsic impurities (carbon (C) from plasma-facing components (PFCs) and oxygen (O) from residual water and air leaks), modify fuel recycling and improve discharge reproducibility; however, they also create compositionally complex, evolving mixed-material layers whose spatial non-uniformity and temporal sequencing can strongly influence impurity migration pathways [5, 6]. Progress in predictive PWI and impurity-transport modeling requires quantitative, spatially and depth-resolved constraints on near-surface elemental inventories and film stratification under device-relevant conditions, ideally supported by diagnostics that are compatible with in-vessel deployment and can provide timely feedback during campaigns. In-vessel analysis under vacuum or inert gas conditions prevents the oxidation of material surfaces post extraction from the magnetically confined device.

Wendelstein 7-X (W7-X) is an advanced stellarator designed with a three-dimensional (3-D), five-fold modular geometry, which is equipped with graphite divertors, heat shields and baffles. During the first two experimental campaigns (operation phase OP1.2a and OP1.2b), W7-X operated with 10 inertially cooled island Test Divertor Units (TDUs) which were extracted and replaced by actively cooled CFC modules for campaign 2.1. In the OP1.2b campaign, the device conducted a total of 9054 s of hydrogen (H) and limited helium (He) plasma discharges, along with boronization of the wall conditioning and the injection of ^{13}C-marked methane ($^{13}CH_4$) in the last phase of the campaign [7, 8].

Boronization is routinely employed in magnetic confinement devices to getter O and reduce intrinsic impurities levels such as C and moderately reduce hydrogen recycling, resulting in improved plasma performance [9–11]. During W7-X OP1.2b, three boronizations were performed by glow discharge using a 90% He and 10% diborane (B_2H_6) mixture. The injected gas amounts were 45, 84 and 68 bar·L of He-B_2H_6 mixture during 3.5, 5.5 and 5 h, respectively [12]. The corresponding B_2H_6 mass was estimated as 22.85 g and the amount of boron (B) introduced was about 17.86 g. In addition, partial *in situ* boronization during plasma operation was conducted using a B injector, with 2 g of B_4C powder injected, corresponding to about 1.6 g of B [13]. Boronization reduced the divertor O/H flux ratio by ∼10× (C/H by ∼4×) after the first application and achieved >100× lower O levels after the third, concomitant with a markedly widened operational window (line-integrated density and stored energy) and a reduction of Z_{eff} Mass spectrometry further showed reductions in CO and CO_2 partial pressures by factors of ∼8 and ∼12, implying that pre-boronization C erosion was largely mediated by O-driven CO/CO_2 formation and was suppressed once O was gettered by B [12]. Based on the effects of boronization [12, 14], it is essential to investigate the PWI process involving B and its migration. Additionally, evaluating how the non-uniform distribution and lifetime of B on PFCs impact the efficiency of O and C impurity gettering in the plasma is also significant.

To simulate the erosion of the ^{12}C graphite divertor and subsequent C migration, $^{13}CH_4$ was introduced via two gas injection valves in a single module of the lower TDU during 30 consecutive and similar plasma discharges in the final plasma experiment of OP1.2b. A total of $(4.0 \pm 1.2) \times 10^{22}$ molecules were injected during a series of hydrogen plasmas in the standard magnetic divertor configuration [4]. In addition to W7-X, the use of ^{13}C to study the migration and deposition processes of C has also been carried out in tokamaks such as DIII-D, TEXTOR, JET, and EAST [15–18]. Utilizing diagnostic methods to determine the deposition distribution of ^{13}C provides direct experimental data for benchmarking various simulation codes, such as ERO2.0 and WallDYN [19–21]. For the $^{13}CH_4$ injection experiment in W7-X, such a benchmark was done using *ex situ* nuclear reaction analysis (NRA) [22].

The spectroscopy diagnostic methods based on laser ablation have unique advantages in characterizing fuel (H in W7-X), impurities such as B and O, as well as isotopes (e.g., H, deuterium (D), tritium (T), ^{12}C, ^{13}C) [23–26]. As an atomic spectroscopy technique, laser-induced breakdown spectroscopy (LIBS) has been rapidly developed in the field of surface element analysis of PFCs in recent years due to

its advantages of non-contact measurement, unlimited sample size, and fast, 3D analysis [27–29]. At the same time, based on the ability of real-time and online measurement and simultaneous analysis of multiple elements, *in situ* LIBS technology has been applied to TEXTOR, EAST, JET, WEST, FTU and other fusion devices [30–35]. However, there are few reports on LIBS measurements of the B distribution on the surface of PFCs. Some analysis results from tokamak devices such as TEXTOR and KSTAR have confirmed that nanosecond (ns)-LIBS is capable of measuring B and its distribution characteristics [36, 37]. Compared with ns-LIBS, picosecond (ps)-LIBS is considered more suitable for depth distribution analysis of B-containing thin films, as it can reduce the heat-affected zone of the target, among other advantages. Zhao *et al* were the first to use picosecond LIBS (ps-LIBS) to obtain the B distribution characteristics on the surface of the W7-X divertor, but to improve the detection limit (LOD) of B in LIBS, this measurement was conducted in 1 mbar He environment [26]. Nevertheless, future *in situ* and real-time measurements in-vessel typically require LIBS to operate under vacuum conditions of $\sim 10^{-7}$ mbar. In our previous work, the spectral intensity evolutions of B layers under different laser spot sizes using ps-LIBS were investigated, aiming to optimize the detection sensitivity of B under 10^{-7} mbar [38]. The LODs for B layer thickness and areal density on tungsten (W) substrates were determined to be 2.59 nm and 3.10×10^{16} atoms cm^{-2}, respectively. The agreement between magnetron-sputtered reference films and boronized W7-X samples, which were positioned on the manipulator head only for the duration of boronization, together with the established quantitative calibration curve, enables rapid *in situ* assessment of B layer thickness and lifetime at different locations in fusion devices [39]. For isotope differentiation and measurement, LIBS has the capability to diagnose hydrogen isotopes (H_α, D_α, T_α) when equipped with a high-resolution spectrometer [40]. For instance, Favre and Harilal used LIBS to conduct depth profile measurements on thin-film samples and neutron-irradiated Zircaloy-4 samples, respectively, directly confirming the ability of LIBS to measure T [41, 42]. However, when measuring heavier atomic nuclei, such as C, the isotope shift is too small, making it challenging for the spectrometer to distinguish between isotopes. To address this, LAMIS has been proposed to detect spectra emitted by diatomic molecules like C_2, CH, and CO in laser-ablated plasma [43, 44]. In practice, LAMIS can usually only obtain the spectral band peaks of diatomic molecules at higher ambient pressure (>1 mbar). The detection capability of LAMIS for isotopic molecular spectra under 10^{-7} mbar remains to be verified.

This work aims to obtain the spatial distribution of C, B, H, and O elements on the W7-X divertor target elements (TEs) close to the $^{13}CH_4$ injection location using ps-LIBS under 10^{-7} mbar. Subsequently, the elemental distribution characteristics measured by ps-LIBS are compared with the results from NRA and LAMIS. A contact profilometer was used to determine the depth ablation rate of the co-deposited layer and graphite substrate, allowing the depth distribution profiles of C, B, H, and O at different locations to be obtained. Additionally, through standard sample calibration, the depth distribution evolution of the B/C content and retained B inventory on the tiles was estimated using ps-LIBS. Furthermore, the surface morphology, co-deposited layer thickness, and elemental depth profiles at several typical positions of the tiles were determined using FIB-SEM and EDS. Finally, XPS was also employed to characterize the elemental content and chemical bonding composition at a 10 nm depth on the tile surfaces.

2. Sample acquisition and experimental setup

2.1. Sample acquisition after the OP1.2b campaign from W7-X device

After the OP1.2b campaign, the inertially cooled TDU was disassembled for post-mortem analysis, providing an excellent opportunity to obtain the elemental distribution characteristics of the PFCs surface.

The W7-X has five toroidal sections, each containing upper and lower TDU units. There are a total of 10 half modules (HMs) and each HM consists of a vertical target (VT) and a horizontal target (HT). Each TDU is divided into several target modules (TMs), with each TM consisting of up to 12 TEs made from pyrolytic graphite. The schematic diagram of the HM39 (which is equipped with two adjacent $^{13}CH_4$ gas injection nozzles), strike line pattern of impinging plasma particles and the magnetic field lines in standard magnetic configuration are shown in figure 1. The number 39 represents the lower TDU unit in section 3. The gas nozzles were positioned between TEs TE4 and TE5 of divertor module HM39TM2h. The letter h represents the horizontal target. In this work, the TE2 of HM39TM2h and TE2 of HM39TM3h on both sides of the gas nozzles were used for characterization and analysis, and their specific locations are shown in figure 2. After the extraction at the end of OP1.2b from the W7-X vessel, the TEs were cut into smaller blocks (10 mm toroidal × 25 mm poloidal × 5 mm thickness) along poloidal direction to be suitable for measurements using NRA technology [22]. Figure 2 illustrates the analysis directions and positions of different techniques. NRA was first used for analysis, followed by LIBS and LAMIS techniques. Due to the limited spectral coverage of a single measurement, LIBS was performed three times to obtain the distribution of O, H, and B elements. The space interval between each column of scans was approximately 1 mm in the toroidal direction and 2.5 mm in the poloidal direction. The beam spot diameter of NRA was approximately 200 μm, while the ablation crater diameters for LIBS and LAMIS were about 480 μm. The pumping gap is set to $s = 0$ mm in the poloidal coordinate system. In addition, as shown in figure 2, a series of laser ablation craters with different numbers of pulses was produced near the poloidal position $s = 240$ mm on TM3hTE2 to calibrate the depth ablation rate of LIBS.

2.2. LIBS experimental setup

Figure 3 illustrates the experimental setup of the ps-LIBS system. A third harmonic wavelength (355 nm) Nd: YAG laser (EKSPLA, PL2241) with pulse-width of 35 ps was used to ablate the samples and generate plasma. The laser was directed

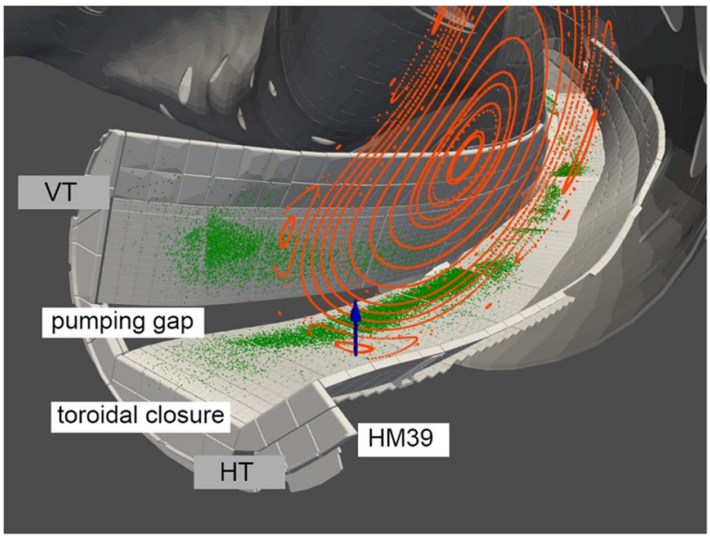

Figure 1. The schematic diagram of the HM39 with horizontal and vertical target (HT/VT), strike line pattern of impinging plasma particles in green and magnetic field lines in red and the injection nozzles in blue. The injection nozzles appear as a single arrow due to the short distance between them.

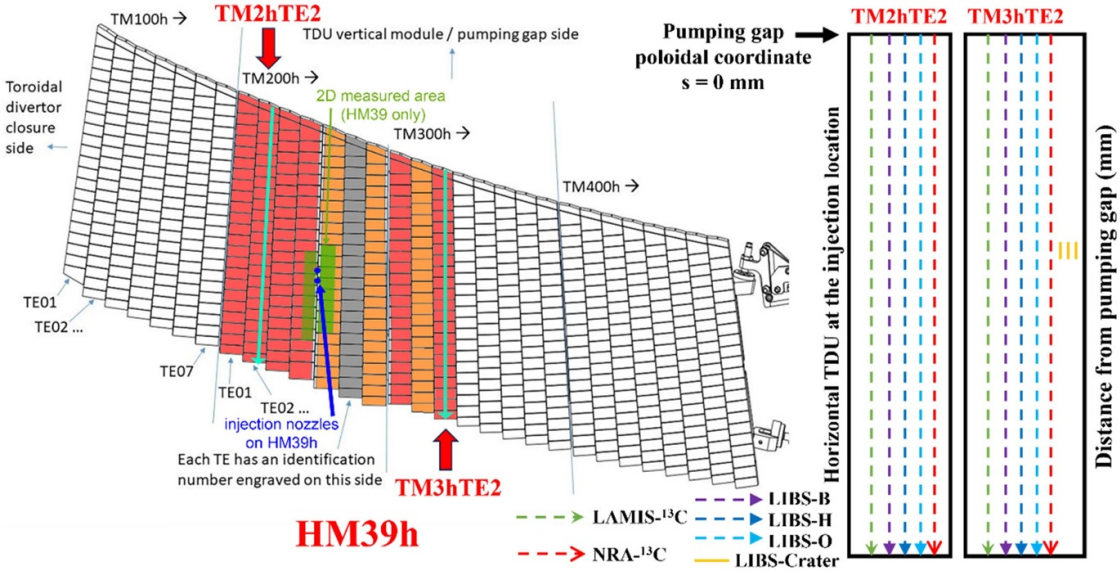

Figure 2. The position of the TM2hTE2 and TM3hTE2 on HM39h analyzed by LIBS, LAMIS and NRA. The pumping gap is set at $s = 0$ mm in the poloidal coordinate system. A series of laser-ablation craters was produced to calibrate the LIBS ablation rate and the corresponding pulse-to-depth conversion.

through two mirrors and two apertures, and then focused onto the sample surface inside the vacuum chamber using a lens with a focal length of 500 mm and a diameter of 50 mm. The focus of the laser was positioned slightly behind the sample surface. The samples were mounted on a two-dimensional translation stage for spatial scanning. The emission light of laser-induced plasma passed through an optical quartz window and then was coupled into an optical fiber (NA: 0.22) with core diameter of 1.5 mm via a lens with a focal length of 250 mm and a diameter of 75 mm. A multi-notch filter (355 nm, 532 nm,1064 nm) was placed in front of the fiber, which was used to block the scattered light from the laser and to protect the ICCD detector. The other side of the fiber was connected to a spectrometer (F-number: 4.3) with a Littrow configuration equipped with an ICCD camera (iStar DH334T-18F, Andor). Due to the spectrometer having a wavelength coverage range of approximately 13 nm, a 1200 grooves/mm grating was rotated three times to detect elements such as B, H, and O. The synchronization between the pulsed laser and the spectrometer was controlled by a digital delay generator (DG645, Stanford R.S.). A computer was used to control the spectrometer for element detection and to manage the motors for spatially resolved measurements.

To simulate the vacuum environment of W7-X, the pressure inside the vacuum chamber was maintained at approximately 3×10^{-7} mbar using a combination of a rotary and

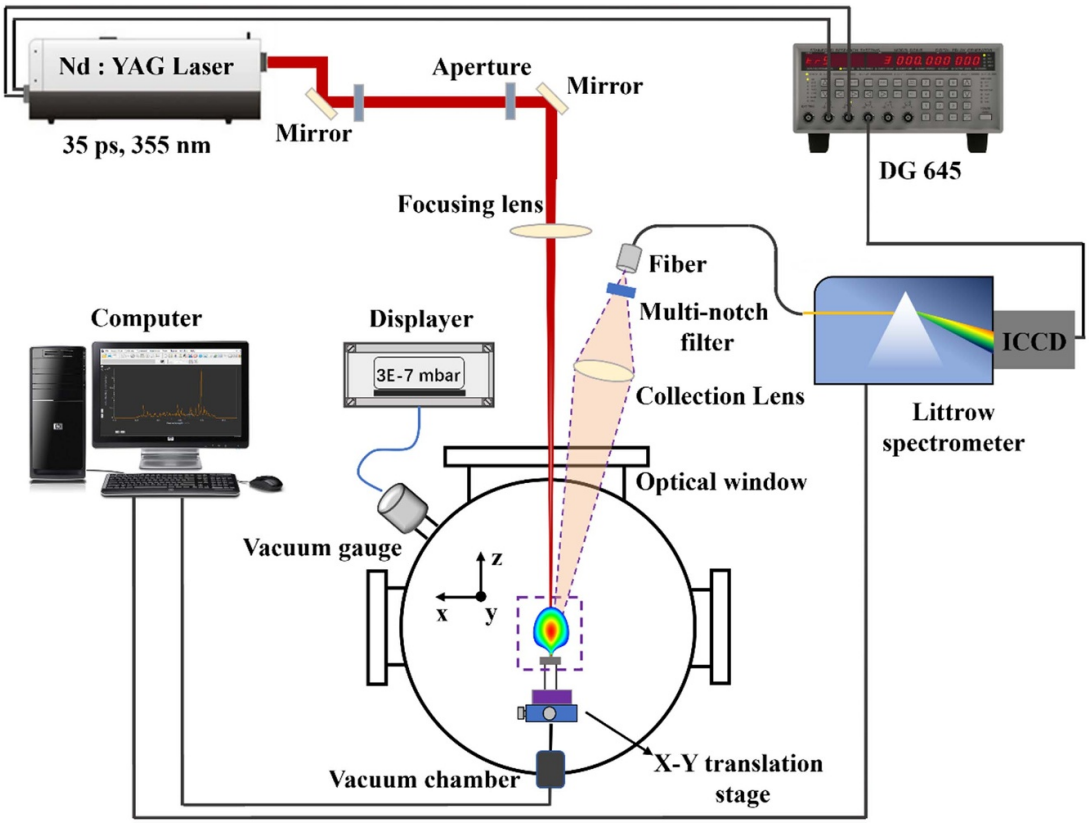

Figure 3. Schematic diagram of the LIBS experimental setup.

a turbo-molecular pump, and LIBS measurements were conducted under these conditions. The pressure inside the chamber was monitored by a vacuum gauge in real-time. It is important to note that the only difference between the LIBS and LAMIS measurements in this work is the variation in pressure and acquisition time. When using LAMIS to measure the molecular spectra emitted by the laser-induced plasma, the chamber was filled with pure N_2 to maintain a pressure of about 1 mbar. The gate delay time and integration time for the LIBS measurements were set to 50 ns and 500 ns, respectively. For LAMIS spectral acquisition, a gate delay of 300 ns and an integration time of 30 μs were used. The laser energy was fixed at 18 mJ. In our previous work, the optimal B signal measured by ps-LIBS at 10^{-7} mbar was obtained with a spot size ranging from 450 to 650 μm, corresponding to an energy density range of 5–11 J cm^{-2} [38]. Therefore, the laser spot diameter of this work was fixed at approximately 480 μm, and the laser energy density was about 9.95 J cm^{-2}.

The characteristic line intensities I were obtained by numerically integrating the emission peaks after subtracting a local continuum baseline. For depth profiles, the spectrum acquired after each laser pulse was used to represent the signal at the corresponding ablation depth, with the pulse-to-depth conversion based on the ablation-rate calibration. Reported uncertainties (e.g. calibration factor and ablation rates) correspond to the fitting errors from the least-squares regressions used in the calibrations.

3. Results and discussion

3.1. Typical spectra and two-dimensional distribution of elements measured by LIBS

The typical spectra of TM3hTE2 measured by LIBS change with the number of laser pulses under simulated W7-X vacuum conditions, as shown in figure 4. This measurement location is $s = 240$ mm away from the pumping gap. The characteristic spectral lines of B II-703.0 nm, 703.2 nm and 703.3 nm, H I-656.3 nm, O I-777.2 nm, 777.4 nm and 777.5 nm, and C II-657.8 nm, 658.3 nm and C I-784.0 nm are clearly visible under the 3rd laser pulse. This demonstrates the feasibility of ps-LIBS for detecting B and other fuel/impurity elements under vacuum conditions relevant to magnetically confined plasma devices ($\sim 10^{-7}$ mbar), indicating future in-vessel implementation of LIBS. As the number of laser pulses increases, the measurement region of the LIBS becomes progressively deeper with the removal of the surface material. The spectral line intensities of B, H, and O decrease significantly by the 8th laser pulse, and after the 30 cumulative laser pulses, the spectral intensities of these three elements fall below the LOD of the current experimental system. The spectral line intensity measured by LIBS is directly related to the elemental concentration. Therefore, B, H, and O are primarily deposited on the tile surfaces, while C is present in all laser pulses, originating from both the ^{12}C graphite substrate and the deposited ^{12}C/^{13}C-containing layers. Based on

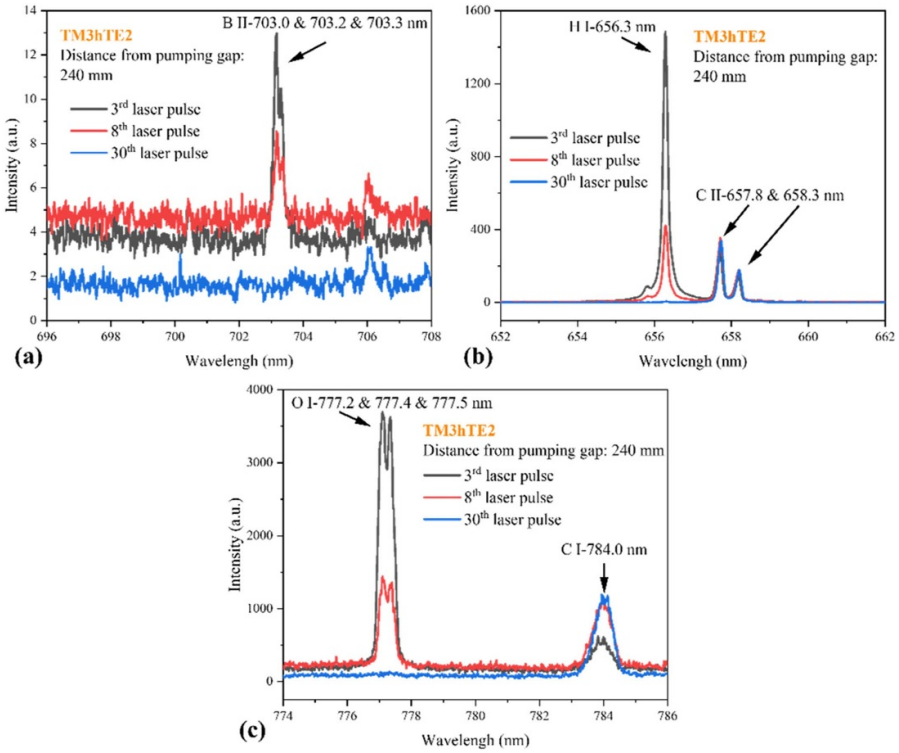

Figure 4. The variation of LIBS spectra for (*a*) B II-703.0/703.2/703.3 nm, (*b*) H I-656.3 nm, and (*c*) O I-777.4 nm under different numbers of laser pulses. The spectra measured at poloidal position $s = 240$ mm away from the pumping gap in TM3hTE2.

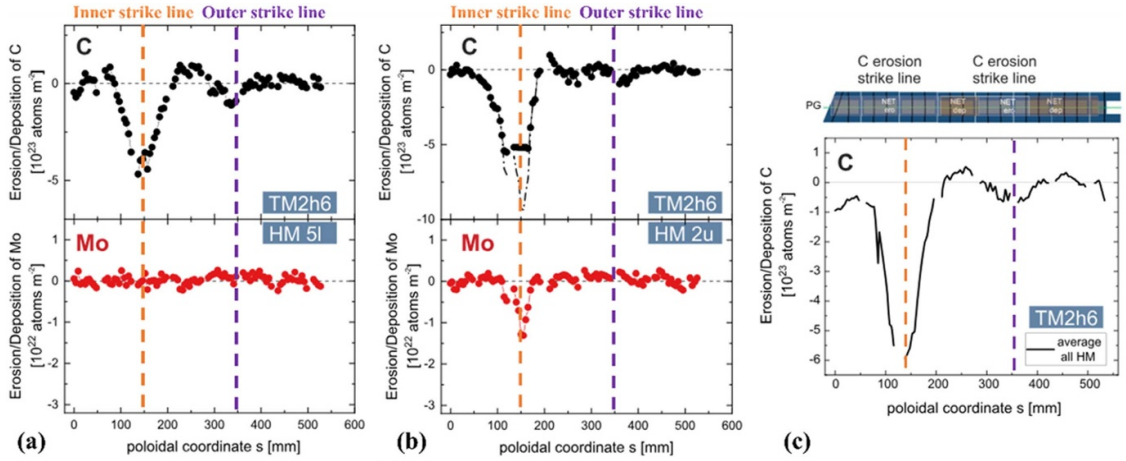

Figure 5. The net C erosion/deposition pattern along the poloidal coordinate s for the horizontal target element TM2hTE6 measured in (*a*) lower half module 59 (HM5l) and (*b*) upper half module 28 (HM2u). (*c*) The averaged poloidal net C erosion/deposition profiles of all ten half modules of the TDU. The inner and outer strike lines are indicated, together with the corresponding regions dominated by net erosion and net deposition. Reproduced from [4].

the spatial scanning capability of LIBS, a systematic characterization of the two-dimensional distribution of B, H, O, and C on the surfaces of TM2hTE2 and TM3hTE2 was subsequently performed.

Figures 5(*a*) and (*b*) present our previously measured net erosion and deposition pattern along the poloidal coordinate *s* on the horizontal TEs of TM2hTE6 for two representative half modules, namely the lower half module 59 (HM 5 l) and the upper half module 28 (HM2u), after OP1.2b plasma exposure [4]. Positive values indicate net deposition, corresponding to a net increase in surface material after plasma exposure, whereas negative values indicate net erosion, corresponding to a net loss of surface material. Therefore, the erosion/deposition pattern shown here represents the accumulated net effect of erosion, re-deposition, and possible re-erosion processes during the OP1.2b plasma exposure. These previously reported profiles are included here as a reference to indicate the strike-line locations and to guide the identification of erosion- and

deposition-dominated regions relevant to the present LIBS and LAMIS analysis. The coordinate s is referenced to the pumping gap of the horizontal target. For both HMs, the strongest net erosion occurs at approximately $s = 150$ mm, coinciding with the inner strike line in the standard divertor configuration. A second erosion feature with substantially lower magnitude appears further downstream at about $s = 350$ mm. This location corresponds to the secondary strike line on the horizontal target in the standard configuration and overlaps with the main strike line of the low iota configuration, which accounted for only about 13% of the OP1.2b operation time, compared with roughly 53% for the standard magnetic divertor configuration. In addition, distinct net-deposition regions are observed adjacent to the inner strike line close to the pumping gap and in the interval between the two erosion dominated zones. For comparison, figure 5(*c*) shows the poloidally averaged net C erosion and deposition profile obtained by combining the results from all ten HMs exposed during OP1.2b.

The poloidal distribution of normalized LIBS intensity for B, H, O, and C elements on TM2hTE2 and TM3hTE2 surface are shown in figures 6(*a*) and (*b*). Here, 'surface' refers to the near-surface region probed within the first 20 laser pulses, after which the graphite substrate is reached at all investigated positions. For each poloidal position, the spectral line intensity of a given element was integrated over the investigated depth, corresponding to the first 20 laser pulses. The resulting integrated intensity was then normalized to the maximum intensity of that element to highlight its relative variation along the poloidal coordinate s. Although no dedicated marker layers such as W or Mo are present on these graphite tiles, which prevents a direct quantification of the eroded thickness, the net-erosion and net-deposition regions can still be inferred from the complementary behavior of deposited species and the substrate element C. Two net-erosion regions are apparent, one near the inner strike line at $s = 120$ mm to $s = 200$ mm and another near the outer strike line at $s = 325$ mm to $s = 375$ mm, in agreement with the erosion and deposition pattern reported in figure 5. Co-deposition regions are observed on both sides of the erosion-dominated zones. Overall, B, H, and O exhibit broadly similar poloidal trends, but with distinct differences in peak locations and amplitudes. The B deposition is most prominent in the region between the two strike lines, while the H and O deposition display a strong peak near the outer strike line on TM2hTE2 and two pronounced peaks near the outer strike line on TM3hTE2. In addition, the distribution characteristics of TM2hTE2 and TM3hTE2 elements are also slightly different, such as the width of the deposition region between the two strike lines. This may be related to the topology of the magnetic field lines and the connection length. The strong deposition peaks of H and O near the outer strike line are likely associated with the injection of $^{13}CH_4$ during the final plasma experiment of OP1.2b in W7-X.

The depth-resolved behavior is illustrated in the two-dimensional LIBS maps in figures 6(*c*)–(*j*), which display the signal intensity as a function of poloidal distance and pulse number. As mentioned above, B, H, and O signals are mainly associated with near-surface deposits and are therefore concentrated within the first 20 laser pulses. The enhanced H and O signals in the very first pulse at the topmost surface are largely attributed to post-exposure effects, namely adsorption of water and surface oxidation after air exposure. Except for the localized deposition peak near the outer strike line, the depth evolution of B, H, and O is largely correlated, indicating co-deposition in the main deposition zones. In particular, the B-rich deposition band between $s = 220$ mm and $s = 320$ mm is dominated by the first few pulses, with B largely confined to the first three pulses and becoming negligible after about 10 pulses. A distinct stratification is observed at the deposition peak near the outer strike line. On TM2hTE2, near the $s = 405$ mm, the B signal is mainly concentrated between the 4th and 8th laser pulses, indicating a deeper B-containing layer than in the $s = 220$ to $s = 320$ mm region. In contrast, at $s = 405$ mm, the intensity of H and O element is strongest in the first few laser pulses and remains detectable beyond 15 laser pulses. A comparable trend is also observed for the two deposition peaks near the outer strike line on TM3hTE2, located at $s = 325$ mm and $s = 393$ mm. It should be noted that the tiles were measured by LIBS under a vacuum of about 10^{-7} mbar to minimize the influence of residual water vapor and ambient gases on the H and O detection. Among the measured species, the B and C distributions provide the clearest indication of erosion and deposition zones. Nevertheless, because the tiles were removed from the device and stored in air for an extended period, the H and O signal in the outermost surface layer represents a combination of surface contamination and oxidation. The H and O behavior below the topmost surface layer is therefore more representative of the in-vessel erosion, transport, and deposition processes in W7-X.

After several boronizations and long-time plasma discharges, the fuel H and impurity elements such as B and O particles undergo complex PWI processes, leading to erosion or deposition on the tile surfaces of the divertor. The B, H, O, C, and other elements primarily concentrate on the surface layer of the tiles. However, in the final plasma experiment of OP1.2b, two gas nozzles located between the divertor module TEs TM2hTE4 and TM2hTE5 injected $(4.0 \pm 1.2) \times 10^{22}$ molecules of $^{13}CH_4$. The break-up of the methane is complex and a fraction of the injected $^{13}CH_4$ likely breaks up rapidly after injection. Some CH_x radicals stick near the injection location and others are ionized CH_x molecules, which are transported along the strike lines and the magnetic islands, eventually depositing on the tile surfaces. The NRA measurements of ^{13}C indicate that, excluding the 10 cm diameter region at the gas nozzle position, a total of approximately 8.7×10^{21} (23% of the injected amount) ^{13}C atoms were extracted from the horizontal target of HM39 [22]. The deposited ^{13}C mixed layer may contain hydrocarbon or carbon-oxygen chemical bonds, as demonstrated in section 3.5. Therefore, a new mixed layer of C, H, and O will deposit on top of the original B-containing mixed layer, ultimately resulting in the

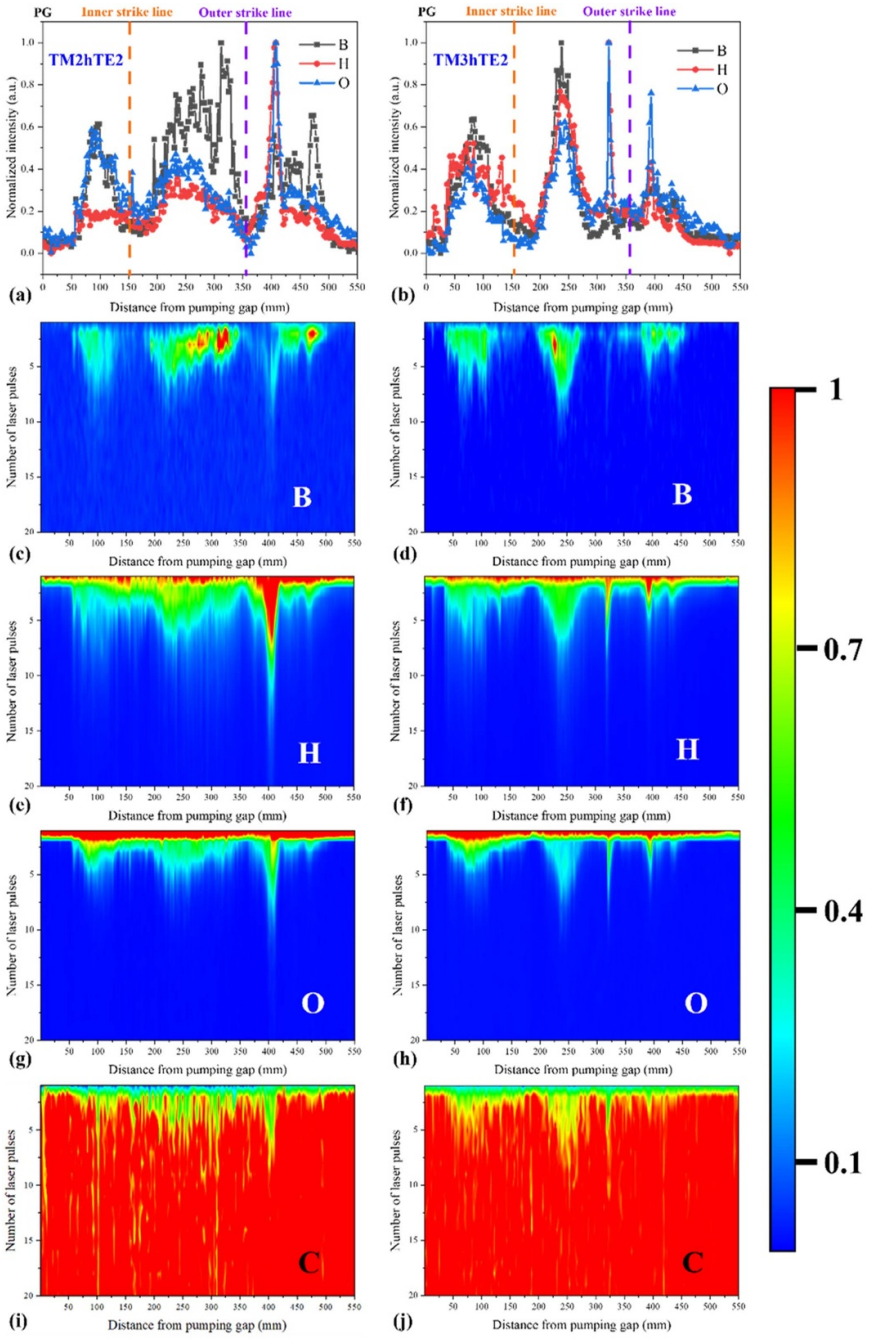

Figure 6. Poloidal distributions of the depth-integrated, normalized LIBS intensities of B, H and O on (*a*) TM2hTE2 and (*b*) TM3hTE2. Each point represents the spectral intensity integrated over the investigated depth. Depth-resolved LIBS intensity maps as a function of poloidal coordinate s from the pumping gap and pulse number for (*c*), (*d*) B, (*e*), (*f*) H, (*g*), (*h*) O and (*i*), (*j*) C on TM2hTE2 and TM3hTE2, respectively. The inner and outer strike lines are indicated by the dashed lines in (*a*) and (*b*). For the two-dimensional LIBS intensity maps in (*c*)–(*j*), each panel is independently normalized to its own maximum intensity, and the color bars therefore represent relative LIBS intensities in arbitrary units.

unique phenomenon of a strong deposition peak near the outer strike line. Notably, the final boronization was performed long time before the last experiment of OP1.2b. Simultaneously, due to the transport along the magnetic islands occurring only in the counterclockwise direction in the toroidal plane, the net migration and deposition along the magnetic islands have a preferred direction away from the divertor closure. Nevertheless, the strike line peaks exist in both directions. This results in significantly higher ^{13}C deposition near $s = 405$ mm on TM2hTE2 than near $s = 325$ mm and $s = 393$ mm on TM3hTE2. The migration behavior of ^{13}C has been discussed in detail in our previous work [22]. Subsequently, the distribution characteristics of H and O along the poloidal direction measured by LIBS on TM2hTE2 and TM3hTE2 were compared with the results obtained from NRA and LAMIS.

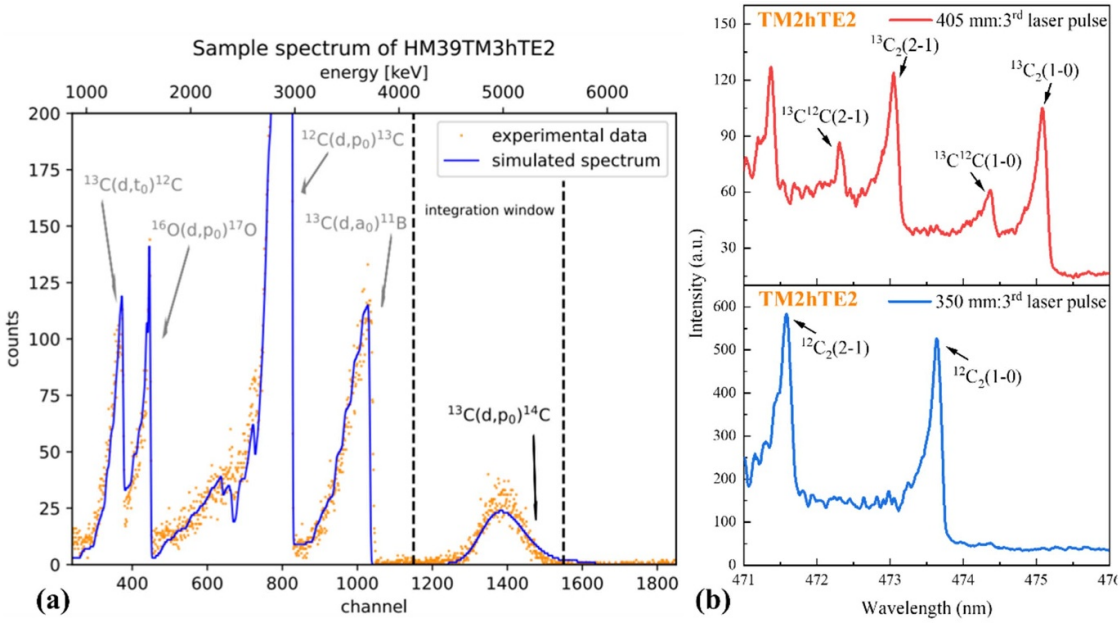

Figure 7. (*a*) Typical spectra of ^{13}C, ^{12}C, and ^{16}O measured by NRA on TM3hTE2 [22]. (*b*) Comparison of the spectra with and without ^{13}C, measured by LAMIS at $s = 405$ mm and $s = 350$ mm away from the pumping gap on TM2hTE2, respectively.

3.2. Comparison of the measurement results between LIBS, NRA, and LAMIS

Figure 7(*a*) presents the typical spectra of ^{13}C, ^{12}C, and ^{16}O measured by NRA on TM3hTE2. The sample was irradiated with 1.00 MeV D^+ ions as the standard energy for the projectile. SIMNRA (v. 7.03) was used for stack correction and provided spectral forward simulations based on the given beam parameters and assumed layer compositions [45]. The ^{16}O(d, p$_0$)^{17}O and ^{13}C(d, p$_0$)^{14}C reactions were used to evaluate the thickness and content of the layers containing ^{16}O and ^{13}C, respectively. Figure 7(*b*) presents a comparison of the spectra measured by LAMIS with and without ^{13}C under the 3rd laser pulse at $s = 405$ mm and $s = 350$ mm on TM2hTE2. After the chamber in figure 3 was filled with N_2 gas and the pressure stabilized at 1 mbar, the grating was rotated so that the wavelength range of the spectrometer covered 467 nm to 481 nm to observe the 1–0 vibrational band of the C_2 Swan system ($d^3\Pi_g \rightarrow a^3\ \Pi_u$ transition). It can be seen from the spectra that the ^{13}C^{12}C molecular bands (474.10–474.60 nm) and $^{13}C_2$ molecular bands (474.83–475.73 nm) are clearly observed at the ^{13}C-rich location of $s = 405$ mm. In contrast, at $s = 350$ mm position, only $^{12}C_2$ molecular band (473.37–473.87 nm) is detected. The work of Kawan and Wüst provides a detailed description of the steps involved in the data processing and analysis of NRA and LAMIS [22, 46].

The results of H measured by LIBS are compared with those of ^{13}C measured by NRA and LAMIS, as shown in figures 8(*a*) and (*b*). On both TM2hTE2 and TM3hTE2, the deposition peaks of H and ^{13}C near the outer strike line match quite well. Since the intensity distributions of H and ^{13}C are both normalized, it is found that, except for the deposition peak near the outer strike line, the distribution characteristics of H in other deposition regions differ significantly from the distribution trend of ^{13}C, with the intensity of H being notably higher than that of ^{13}C. This is reasonable because ^{13}C was primarily injected during the final plasma experiment of OP1.2b, while H is the cumulative result of the entire campaign. Most of the CH_4 molecules, after being dissociated and/or ionized by plasma, deposit as a CH_x mixture on the divertor surface along the strike line and magnetic islands, leading to a significant increase in the H content near the outer strike line on TM2hTE2 and TM3hTE2. As mentioned above, aside from the significant increase in H and O deposition at specific locations due to the injection of $^{13}CH_4$ molecules, the deposition patterns of B, H, and O are largely consistent and indicate co-deposition, except in the outermost surface layer. Based on the above results, the H and O distributions measured before and after $^{13}CH_4$ injection can serve as a qualitative proxy for regions influenced by ^{13}C-bearing co-deposition and the associated PWI processes. Overall, LIBS demonstrates strong capability for H detection, providing an important and comprehensive complement to surface elemental analyses for divertor tiles, which is difficult and challenging for NRA.

In the final phase of OP1.2b, the injection of $^{13}CH_4$ introduces an additional, time-localized impurity source on top of the cumulative boronization and long-duration H plasma exposure. A large fraction of the injected methane is expected to dissociate rapidly, and the resulting ionized and/or dissociated CH_x species migrate predominantly along the strike lines and magnetic islands before depositing on the divertor tiles. This transport picture is consistent with the pronounced deposition peaks observed near the outer strike line and with the increased H and O signals in the same regions. Importantly, the $^{13}CH_4$-driven co-deposition forms a new C–H–O rich mixed layer on top of the pre-existing B-containing layer, which explains

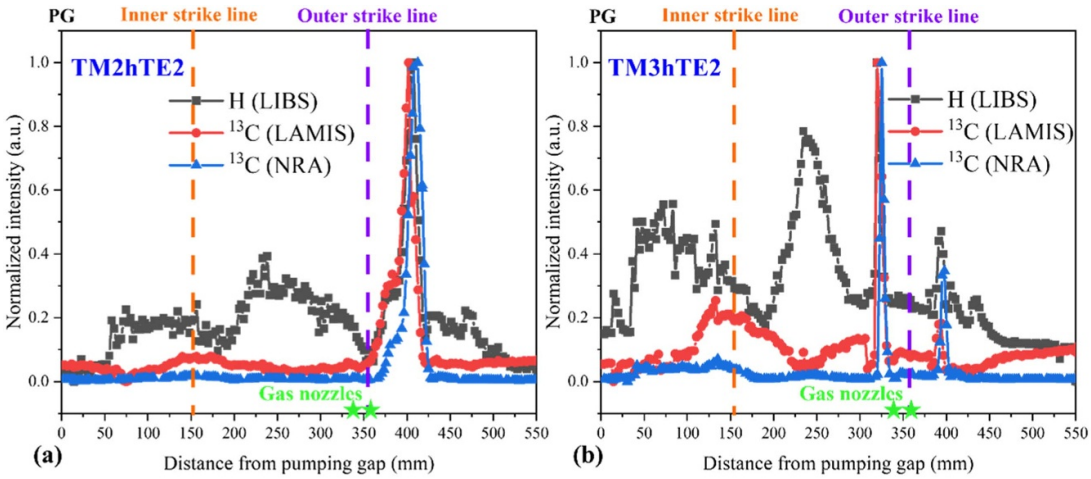

Figure 8. Comparison of the poloidal distribution of H intensity measured by LIBS with the ^{13}C intensity obtained by NRA and LAMIS on (*a*) TM2hTE2 and (*b*) TM3hTE2. The inner and outer strike lines are indicated by the dashed lines, and the two gas injection nozzles' locations are marked by two stars.

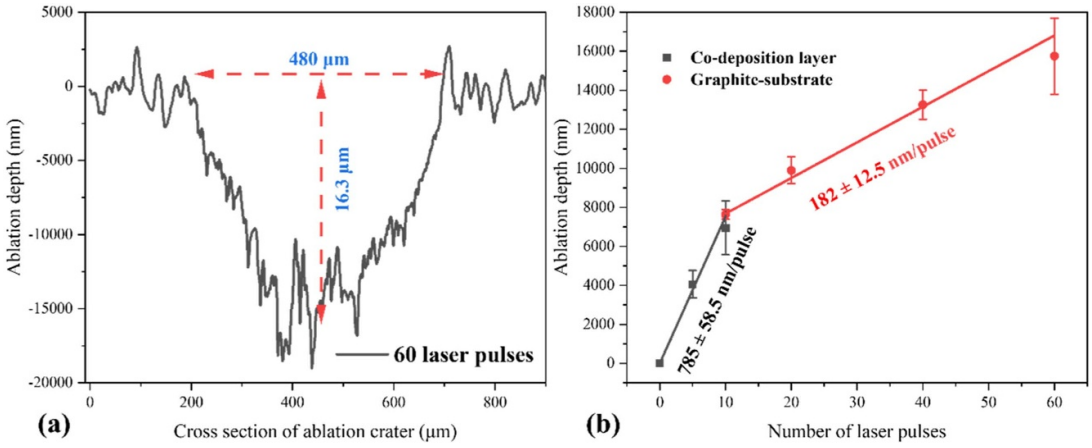

Figure 9. (*a*) Typical profile of ablation crater after 60 laser pulses by LIBS. (*b*) Depth ablation rate of LIBS in the co-deposited layer and graphite-substrate.

why the outer strike-line peak can exhibit shallow H/O enrichment while B can peak deeper in the film. Moreover, because transport along the magnetic islands in the toroidal plane is directional (counterclockwise), the net migration along the islands has a preferred direction away from the divertor closure, while strike-line peaks can occur on both sides. This directional island transport provides a physical constraint for interpreting why the deposition near the $s = 405$ mm region on TM2hTE2 is markedly stronger than the corresponding outer strike-line peaks on TM3hTE2.

3.3. Depth distribution characteristics of elements measured by LIBS

Obtaining the depth distribution characteristics of B, H, and O elements is required to quantify the deposition layer thickness and composition. Due to the different laser ablation rates of the mixed deposition layer and the graphite substrate, calibration and adjustment are required when converting the number of laser pulses into depth characteristics. Figure 9(*a*) presents the typical cross-sectional profile of an ablation crater after 60 cumulative laser pulses at the poloidal position $s = 240$ mm in TM3hTE2. The cross-sectional profiles of ablation craters were measured by a contact profilometer. The diameter of the ablation crater is approximately 480 μm, and the depth is about 16.3 μm. Multiple ablation and measurement experiments were performed near the $s = 240$ mm of TM3hTE2 with different numbers of laser pulses. Independent craters were generated using 5, 10, 20, 40, and 60 laser pulses, respectively. Three repeated columns of ablation craters were prepared and scanned to obtain the average crater depth and the corresponding error bars. The corresponding ablation depths were obtained, as shown in figure 9(*b*). The results show that the variation in ablation depth can be divided into two regions, corresponding to the mixed deposition layer and the graphite substrate. By fitting the ablation depths of both regions using the least squares method, it is found that the average ablation rate of LIBS for the mixed deposition layer

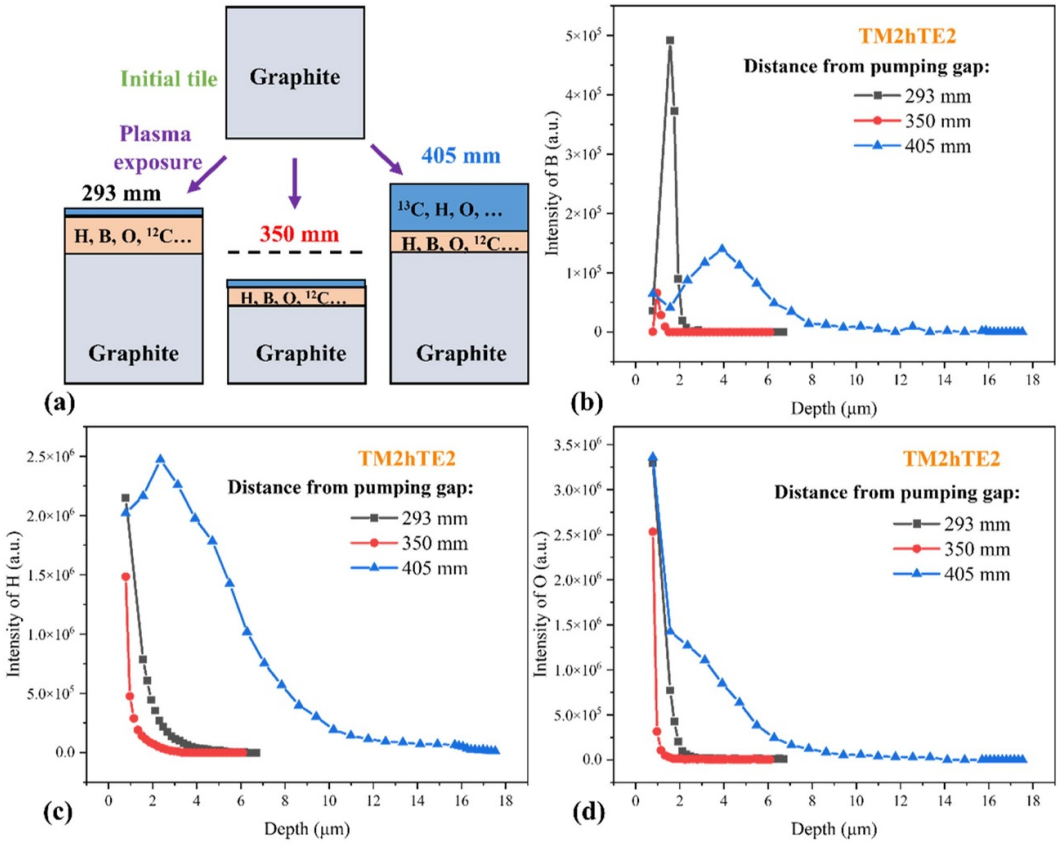

Figure 10. (*a*) Schematic illustration of the layer evolution on the TM2hTE2 graphite tiles after W7-X plasma exposure at three representative poloidal locations. Depth profiles of the LIBS spectral intensities for (*b*) B, (*c*) H, and (*d*) O measured at the same locations. The positions $s = 293$ mm, $s = 350$ mm, and $s = 405$ mm correspond to the region of maximum B deposition, the net-erosion region associated with the outer strike line, and the region of maximum ^{13}C deposition, respectively.

is approximately 785 ± 58.5 nm pulse^{-1} for the given experimental set-up and laser energy, and the graphite substrate is about 182 ± 12.5 nm pulse^{-1}.

The pulse-to-depth conversion is based on profilometry-calibrated average ablation rates for (i) the mixed deposition layer and (ii) the graphite substrate, derived from crater-depth measurements around $s = 240$ mm. The resulting calibration was used to determine the average ablation rates in the mixed deposition layer and in the graphite substrate. While this two-regime calibration captures the dominant change in ablation behavior between film and substrate, the absolute depth scale in thick and compositionally complex deposits should be regarded as an effective depth, because local porosity, bonding state and composition (C–H–O–B mixtures) can alter the ablation efficiency. To mitigate this, the LIBS-derived thickness scale is validated against independent cross-sectional measurements. Specifically, as shown in figure 12, FIB-SEM cross-sections at representative locations (e.g. $\sim$0.9 μm at $s = 293$ mm and 13–17 μm at $s = 405$ mm) confirm the order-of-magnitude thickness differences inferred from LIBS and support the reliability of the depth-resolved trends reported here.

Figure 10(*a*) provides a schematic, qualitative illustration of how the near-surface layers on the TM2hTE2 graphite tile may evolve in different poloidal regions before and after W7-X plasma exposure. The layered structure is drawn for visualization purposes only. Each layer represents a multi-element mixed deposit rather than a chemically pure film, and interactions between successive deposits, including intermixing and partial re-erosion, are expected. The schematic is therefore intended to clarify the dominant trends inferred from the depth-resolved LIBS signals, rather than to imply sharply separated interfaces or strictly sequential deposition. Based on the position-dependent variations in the pulse-resolved elemental signals, the depth axis was reconstructed by applying the corresponding average ablation rates at each location.

Figures 10(*b*)–(*d*) presents the depth profiles of B, H, and O spectral intensity measured by LIBS at three typical positions on TM2hTE2. At $s = 350$ mm, which lies in the net-erosion region associated with the outer strike line, B, H, and O exhibit the lowest overall intensities. The mixed surface layer is also the thinnest and is largely confined to the near-surface region within approximately 0.785 μm. In the net-deposition region between the two strike lines at $s = 293$ mm, all three elements show clearly enhanced signals and a thicker mixed layer extending from about 0.785 μm to 2.355 μm. In contrast, at $s = 405$ mm, corresponding to the region of maximum ^{13}C deposition, the H and O signals are highest and

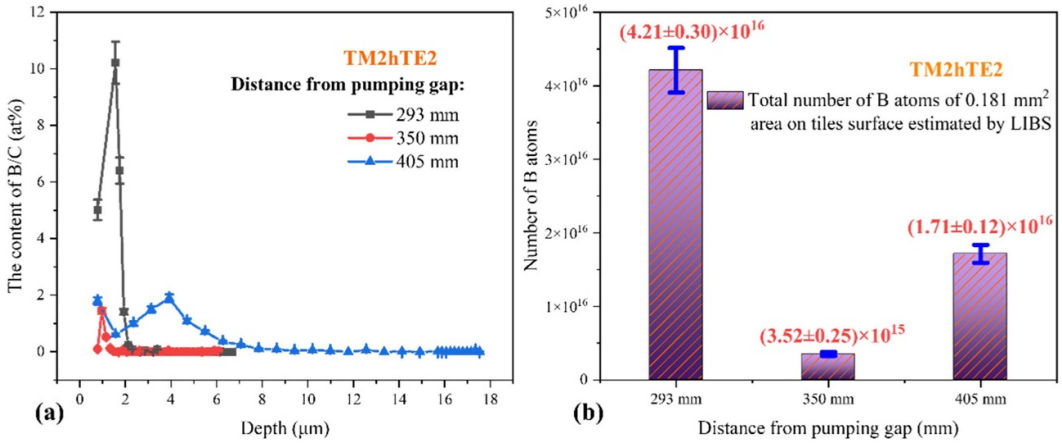

Figure 11. (*a*) Depth distribution profiles of the B/C content ratio and (*b*) total number of B atoms of 0.181 mm^2 area on tile surfaces estimated by LIBS at three typical positions on TM2hTE2.

persist to much greater depths, with the mixed layer thickness exceeding 12 μm. The depth evolution of B, H, and O at $s = 293$ mm and $s = 350$ mm follows similar trends, consistent with co-deposition. A different stratification is observed at $s = 405$ mm. There, H and O peak at the surface and decrease monotonically with depth, whereas B increases initially and then declines, forming a pronounced subsurface maximum at around 4–5 μm. This behavior is attributed to the large injection of $^{13}CH_4$ molecules during the last W7-X plasma experiment with inertially cooled graphite divertor and associated tiles extraction, leading to the deposition of a large amount of H- and O-containing mixture at $s = 405$ mm. The associated top layer partially covers the pre-existing B-containing layer formed earlier in the campaign, thereby shifting the B maximum below the surface and decoupling its depth trend from those of H and O.

Quantification of B from ps-LIBS under device-relevant vacuum is challenged by (i) the limited B signal level in remote collection geometries and (ii) the restricted set of observable B lines and short radiative lifetimes at device-relevant high conditions $\sim 10^{-7}$ mbar and below. To obtain a robust, model-oriented quantification, we calibrate the B/C atomic ratio using a boron carbide (B_4C) reference under identical optical and laser conditions, assuming stoichiometric ablation and proportionality between integrated line intensity and elemental concentration. With the known atomic fraction (B:C = 4:1) in B_4C, the calibration factor k is defined such that the B/C ratio in the co-deposited layer is computed by equation (1),

$$\frac{C_B}{C_C} = \frac{I_B}{4I_C} \cdot k \tag{1}$$

where C_B and C_C represent the atomic contents of B and C, respectively, I_B and I_C are the integral intensities of the characteristic line peaks of B and C measured by ps-LIBS.

Emission from singly ionized B, namely B II-703.0 nm, 703.2 nm and 703.3 nm and C II-657.8 nm lines, were used to obtain the depth distribution profiles of B/C content at three typical poloidal positions on TM2hTE2, as shown in figure 11(*a*). The results show that the content of B is the smallest at the position of $s = 350$ mm and the maximum content per unit depth (1 laser pulse) is less than 1.5%. The content of B per unit depth was the highest at $s = 293$ mm and reaches 10.2% at a depth of approximately 1.57 μm. At $s = 405$ mm, the B content is presented in deeper areas, but the content per unit depth was less than 2%. The pulse-resolved B/C ratio is converted into a pulse-resolved B atomic fraction and is then integrated over the ablated volume removed by each pulse. Specifically, for pulse i, the incremental ablated volume is approximated by $\Delta V_i \approx \pi r^2 \Delta d_i$, where r is the laser ablation crater (240 μm) and Δd_i is the pulse-to-depth increment determined from the ablation-rate calibration (film or substrate regime). Assuming the deposited layer density ρ is close to graphite as a first-order approximation (2.28 g cm^{-3}) and treating the crater as an effective cylinder, the total number of B atoms is estimated by summing over pulses by using equation (2),

$$N = \sum_{i=1}^{n} x_i \frac{\Delta V_i \rho N_A}{M} \tag{2}$$

where N is the total number of B atoms, n is the number of laser pulses, x_i is the B atomic fraction inferred from the B/C ratio at pulse i, N_A is Avogadro's constant (6.022×10^{23}), and M is the relative atomic mass of B (10.81). The dominant systematic uncertainties arise from (a) the unknown exact density of the mixed C–H–O–B layer and (b) deviations of the crater shape from an ideal flat-top cylinder; these contributions are discussed alongside the inventory estimates. After the W7-X OP1.2b campaign, within the spot area measured by LIBS (0.181 mm^2), as shown in figure 11(*b*), on the TM2hTE2, the B deposited amount at $s = 293$ mm could reach $(4.21 \pm 0.30) \times 10^{16}$ atoms, while the B deposition at $s = 350$ mm is approximately $(3.52 \pm 0.25) \times 10^{15}$ atoms. The B deposition at $s = 405$ mm is about $(1.71 \pm 0.12) \times 10^{16}$ atoms. Dhard *et al* assumed

in first approximation a homogeneous boronization procedure and estimated the average thickness of the B/C deposited layer of W7-X to be approximately 70 nm, based on the surface area of the PFCs (192 m^2) and the amount of B introduced by boronization (1.11×10^{24} atoms) [13]. However, this estimate does not include non-homogeneous deposition of B during the boronization using He-GDC and subsequent plasma operation in different magnetic configurations resulting in material migration. Thus, after prolonged W7-X plasma discharges and erosion, transport and deposition processes, the distribution characteristics of B have shown significant differences in various regions, as presented in our results. This is also supported by the findings reported by Mayer *et al* [47]. The pronounced spatial heterogeneity in B retention and co-deposition bears on the efficacy and temporal persistence of wall conditioning. In erosion dominated regions, the B enriched layer remains shallow and of comparatively low areal inventory, consistent with a short effective residence time under continued plasma exposure. Time-resolved spectroscopy indicates rapid strike line B loss, reaching a low steady level after about 59 s of cumulative plasma exposure, corresponding to roughly 15 discharges, consistent with an erosion redeposition balance [12]. Conversely, in deposition-dominated regions the near surface composition exhibits markedly elevated B/C ratios within the top micron, indicative of an enhanced local capacity for O gettering until saturation of the gettering capability is reached. At the same time, an important case is provided by the outer strike line deposition zone, where local hydrocarbon injection at the end of experiment produces a thick C–H–O enriched top layer. This top surface layer partially buries and redistributes pre-existing B. The resulting depth separated stratification, with surface H/O enrichment and a subsurface B maximum, implies that the relevant surface B availability for gettering and recycling control cannot be parameterized by a single, spatially averaged boronization thickness. Rather, it is governed by the local balance between erosion and deposition, strike line dynamics, island-mediated transport, and the temporal sequencing of impurity sources. Boronization benefits, including reduced oxygen influx and impurity radiation, are not uniquely determined by the persistence of an intact B film at the strike line, but by the spatial distribution and effective accessibility of B at plasma exposed surfaces as modified by erosion, redeposition, and co-deposition-driven burial. Therefore, spatially and depth resolved constraints such as those presented here are required to quantify conditioning performance and to benchmark predictive PWI and impurity transport modeling.

3.4. Characterization of TM2hTE2 by FIB-SEM and EDS

Figure 12 depicts the surface morphology and cross-sectional images after focused-ion beam cutting at three typical positions on TM2hTE2, as measured by FIB-SEM. It can be observed that there are obvious differences in surface morphology at the distance of 293 mm, 350 mm and 405 mm poloidally away from the pumping gap. At the same time, the interface between the deposition layer and the graphite substrate is clearly visible. At $s = 350$ mm, compared to the other two positions, the surface morphology appears more uniform and smoother, with no noticeable particle aggregation or large-scale surface defects. The deposited layer at this position is the thinnest, with a thickness ranging from 300.5 nm to 342.1 nm. The net erosion zone has undergone multiple erosion and deposition processes under shallow-angle plasma impact. This may result in a smoothing effect, thereby reducing the surface roughness. At $s = 293$ mm, the surface morphology exhibits relatively flat characteristics, but with some irregular small protrusions. The deposited layer thickness at this position ranges from 897.7 nm to 920.0 nm. At $s = 405$ mm, the surface morphology shows obvious deposition features, with larger particles or structural protrusions on the surface. The deposited layer at this position is the thickest and exhibits significant fluctuations, with a thickness ranging from 13.17 μm to 16.72 μm.

Subsequently, EDS line scans were performed on the cross-section after focused-ion beam cutting, providing the depth profile information of O, C and B content at three typical positions on TM2hTE2, as shown in figure 13. The small residual percentage in the outermost layer is due to the introduction of gallium (Ga) and platinum (Pt) elements during the FIB-SEM measurement. Due to the limitations of EDS, the measurement accuracy for low-Z elements, especially for B in this work, is not high. Therefore, these data provide a reference for evaluating the deposited-layer structure and for comparison with the LIBS-derived depth profiles. At $s = 350$ mm, the O and B content is the lowest, with the thinnest thickness. At $s = 293$ mm, the B content is highest within the top $\sim$1 μm, and due to the strong oxygen affinity of B, O and B exhibit similar behavior. At $s = 405$ mm, the total O deposition amount is large, and the thickness is the thickest, which is also confirmed by the variation of C content with depth. The high O content at larger depths is likely associated with both B–O co-deposition in the pre-existing boronized layer and the formation of a C–H–O-enriched deposited layer during the late-phase $^{13}CH_4$ injection. The LIBS and EDS results show broadly consistent depth-dependent trends, although differences are expected due to their different sampling volumes and measurement mechanisms. In the deposition layer, C is always the dominant element, with a content greater than 75%. The LIBS measurement results are consistent with the FIB-SEM results, further demonstrating the potential of LIBS for *in situ* measurements.

3.5. Compositions and chemical states of TM2hTE2 measured by XPS

In order to investigate the chemical state of the deposited layer on the divertor tiles surface, XPS was used to analyze two typical positions on TM2hTE2 and TM3hTE2. Figure 14(*a*) presents the XPS spectrum measured at $s = 403$ mm on TM2hTE2. The prominent peaks in the spectrum correspond to the C 1s, and O 1s signals near the 285 eV, and 533 eV, respectively. The B 1s signal is also detected near 192 eV,

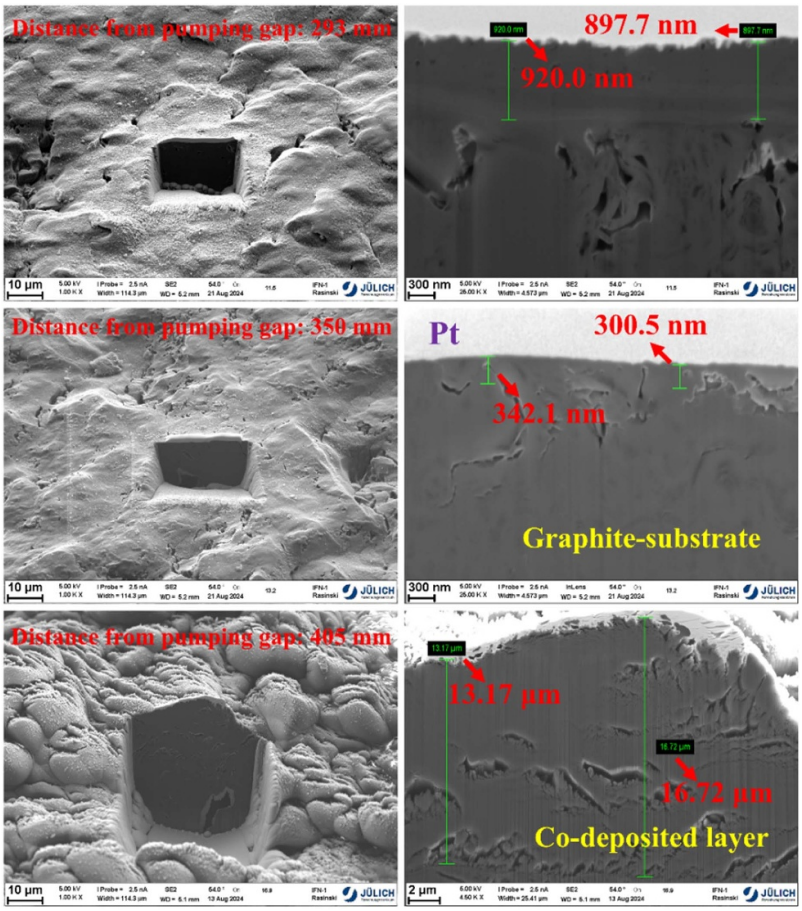

Figure 12. The cross-section of the co-deposited layer on the graphite-substrate at the three typical locations on TM2hTE2 which were analyzed by FIB-SEM.

although its intensity is weaker. The relative atomic contents of B, O, and C within 10 nm of the surface at $s = 403$ mm on TM2hTE2 and $s = 232$ mm on TM3hTE2, as measured by XPS, are illustrated in table 1. The results indicate that C remains the dominant element (>66%) on the surface of the deposited layer. The B and O content at $s = 232$ mm on TM3hTE2 is higher than at $s = 403$ mm on TM2hTE2, which may be because B and O are primarily enriched at the surface at $s = 232$ mm on TM3hTE2.

Figures 14(*b*)–(*d*) present the chemical states of elements within 10 nm of the tile surfaces. The fitting results of the B 1s peak indicate that the B element primarily exists in the form of oxides, particularly boron oxide (B_2O_3). A detailed fitting of the C 1s peak reveals three main sub-peaks: around 284.8 eV for C-C/C-H bonds, around 286.6 eV for C–O bonds, and around 288.4 eV for C=O bonds. This indicates that the sample surface contains various forms of carbon chemical states, possibly including carbon oxides and organic compounds. Figure 14(*d*) depicts the related peaks for C–O and C=O, further confirming the presence of carbon oxides and other oxygen-containing species, with B_2O_3 potentially coexisting with surface organic oxides. These features in the XPS spectra provide important information for analyzing the chemical reactivity and composition of the tile surfaces. Additionally, the presence of hydrocarbons and carbon oxides confirms the characteristic changes on the PFCs surface before and after $^{13}CH_4$ molecule injection, as inferred from the results of H and O measured by LIBS in sections 3.1 and 3.2. However, the shallow information depth of conventional XPS (typically ~10 nm) complicates discrimination between species formed *in situ* during plasma operation and those arising from air exposure/oxidation after tiles removal. To reduce this ambiguity, future work will adopt oxidation-mitigation protocols and conduct ion-sputter depth profiling prior to XPS measurements, providing a clearer picture of the true in-vessel chemical states.

It should be noted that the present measurements are limited to two local horizontal TEs from HM39 near the $^{13}CH_4$ injection region. Therefore, the B inventories obtained here represent local post-mortem values and cannot be directly extrapolated to determine the global fraction of introduced B retained on the full TDU/divertor system as the initial distribution is uncertain. Since boronization was applied to the entire W7-X device, including the first wall, baffles, heat shields, and divertor surfaces, a reliable assessment of the global B distribution requires measurements over a much broader set of PFCs. The

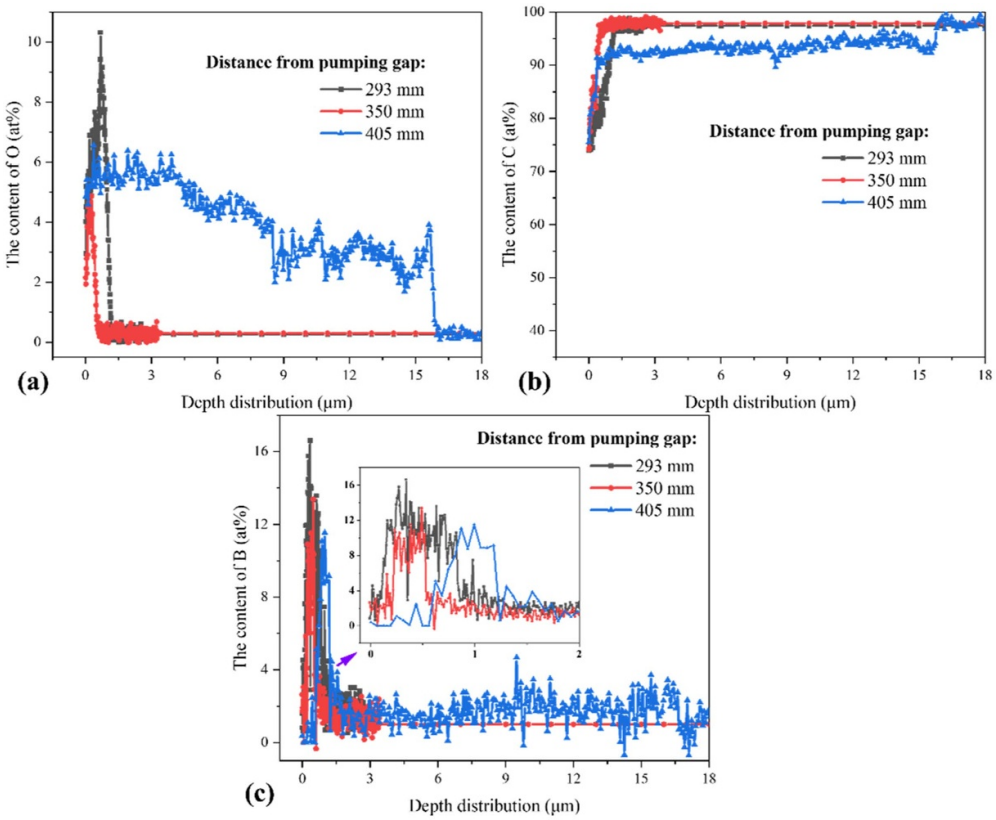

Figure 13. Depth distribution profiles of (*a*) O, (*b*) C, and (*c*) B content at three typical positions on TM2hTE2 which were obtained by EDS.

Table 1. The relative content of B, O, and C on the surface (∼10 nm) at the position $s = 403$ mm poloidally away from the pumping gap on TM2hTE2 and $s = 232$ mm on TM3hTE2.

	Atomic concentration (at%)	
Element	TM2hTE2: $s = 403$ mm	TM3hTE2: $s = 232$ mm
B 1s (192 eV)	0.7 ± 0.08	0.8 ± 0.07
O 1s (532 eV)	26.8 ± 0.50	32.3 ± 0.49
C 1s (285 eV)	72.6 ± 0.51	66.9 ± 0.50

formation mechanism of the measured B-containing layer on the analyzed TDU can be subdivided into (a) direct deposition of boron during the boronization in deposition zones, thus, the boron is deposited by carbon during plasma operation, (b) boron is co-deposited with carbon during normal plasma operation resulting in a mixed layer. TDU surfaces, especially in strike-line and deposition regions, are additionally affected by plasma-driven erosion, re-deposition, co-deposition with C/H/O-containing species, and material migration along the divertor magnetic topology. The B-containing layers observed in this work should therefore be regarded as cumulative mixed-material layers produced by boronization and subsequent PWI processes, rather than as simple as-deposited B films. Future systematic diagnostics of the first wall, baffles, heat shields, and divertor surfaces will be required to clarify the global redistribution and lifetime of B in W7-X. In parallel, analyses of the deposition characteristics of C, B, O, and H, as well as estimates of B inventories on glow-discharge anodes, are currently being carried out. These ongoing and future studies will provide complementary information for evaluating the spatially non-uniform evolution of B-containing layers in W7-X. It should also be noted that self-sputtering, impurity-assisted sputtering, and detachment or impurity-seeding scenarios may influence the erosion/deposition balance on PFCs, particularly on divertor surfaces. Sputtered B-, C-, CH_x-, and CO-containing species may act as local impurity sources and, after dissociation, ionization and transport in the edge/divertor plasma, may contribute to re-deposition, mixed-layer formation, and possible re-erosion. A quantitative separation of these effects from the cumulative post-mortem B/H/O/C distributions is beyond the scope of the present study.

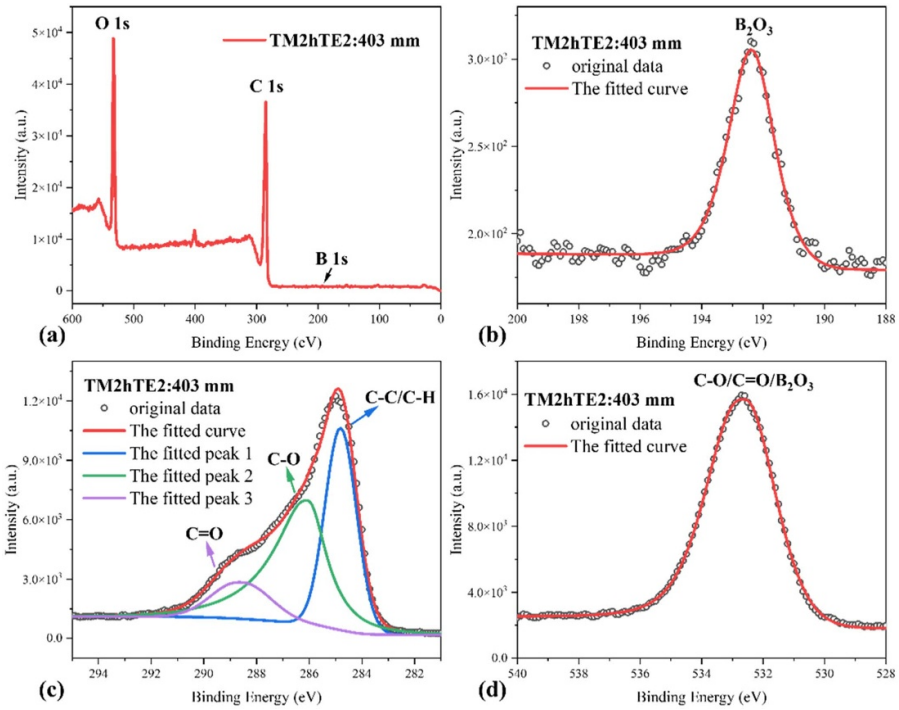

Figure 14. (*a*) Typical spectrum obtained by XPS at a position $s = 403$ mm poloidally away from the pumping gap on TM2hTE2. (*b*)–(*d*) Fitted peaks corresponding to binding energies of chemical bonds in the XPS spectra.

4. Conclusions

This study presents a comprehensive and quantitative assessment of impurity deposition and near-surface evolution on graphite divertor tiles from W7-X following plasma exposure in hydrogen, multiple boronizations, and the end-of-operation $^{13}CH_4$ injection to trace carbon migration. By calibrating the pulse-to-depth conversion via profilometry, ps-LIBS operated under device-relevant high vacuum successfully resolved the poloidal and depth distributions of B, H, O, and C.

The results reveal pronounced spatial heterogeneity in B-H-O co-deposition. The thickness of mixed co-deposited layers range from ∼0.3 to 0.4 μm in erosion-dominated regions (e.g. $s = 350$ mm on the horizontal target in poloidal direction away from the pumping gap), to ∼0.9 μm in B-rich deposition zones (e.g. $s = 293$ mm), and exceeds 12 μm in ^{13}C-rich deposits near the outer strike line (e.g. $s = 405$ mm). These gradients demonstrate the strong influence of magnetic configuration and impurity-source sequencing (e.g. migration vs. injection, boronization) in shaping local retention and film growth.

Using a calibration-based approach, we further quantify B content in a form directly applicable to impurity-transport and co-deposition modeling. The maximum B/C atomic ratio reaches ∼10.2% in the B-rich region of the deposition zone ($s = 293$ mm), whereas it remains below 1.5% in net-erosion areas. The estimated B inventory within a single LIBS crater (∼0.181 mm^2) is $(4.21 \pm 0.30) \times 10^{16}$ atoms in the B-rich region, $(1.71 \pm 0.12) \times 10^{16}$ atoms in the ^{13}C-rich deposition zone, and $(3.52 \pm 0.25) \times 10^{15}$ atoms in the erosion zone. Importantly, LIBS-derived lateral and depth trends are consistent with independent diagnostics (NRA, LAMIS, and FIB-SEM), supporting the robustness of the inferred thickness and compositional distributions. Complementary XPS analysis of the outermost top surface confirms the presence of hydrocarbons, carbon-oxygen species, and boron oxides, underscoring the chemically complex nature of the co-deposited films. The impact of surface oxidation of these *ex situ* samples after extraction from the vessel and exposure to air and moisture is assumed to be moderate and limited to the near surface only.

Overall, these results demonstrate the potential of ps-LIBS for future in-vessel, near-real-time monitoring of surface composition under fusion-relevant conditions without air contamination. ps-LIBS can provide mechanistic insight into how late-stage hydrocarbon seeding can modify and restructure pre-existing boronized layers. The findings advance understanding of PWI processes and inform optimization of wall-conditioning strategies for future fusion devices. Model-ready benchmark observables are provided in the supplementary material, and dedicated modeling and validation work based on these data is currently underway.

Acknowledgments

This work has been carried out within the framework of the EUROfusion Consortium, funded by the European Union via the Euratom Research and Training Programme (Grant Agreement No. 101052200—EUROfusion). Views and opinions expressed are however those of the author(s) only and do not necessarily reflect those of the European Union or the European Commission. Neither the European Union

nor the European Commission can be held responsible for them. This work was supported by the Institute of Energy, Hefei Comprehensive National Science Center (Anhui Energy Laboratory) under Grant No. 25KZS217.

Conflict of interest

The authors declare that they have no known competing financial interests or personal relationships that could have appeared to influence the work reported in this paper.

ORCID iDs

Huace Wu 0009-0007-3037-0132
Christoph Kawan 0009-0008-2784-5245
Sebastijan Brezinsek 0000-0002-7213-3326
Rui Ding 0000-0003-2880-9736
Timo Dittmar 0000-0002-4325-7979
Marcin Rasinski 0000-0001-6277-4421
Gennady Sergienko 0000-0002-1539-4909

References

[1] Lipschultz B. *et al* 2007 *Nucl. Fusion* **47** 1189–205
[2] Knaster J., Moeslang A. and Muroga T. 2016 *Nat. Phys.* **12** 424–34
[3] Linke J., Du J., Loewenhoff T., Pintsuk G., Spilker B., Steudel I. and Wirtz M. 2019 *Matter Radiat. Extrem.* **4** 056201
[4] Brezinsek S. *et al* 2022 *Nucl. Fusion* **62** 016006
[5] Winter J. 1996 *Plasma Phys. Control. Fusion* **38** 1503–42
[6] Krstic P.S., Allain J.P., Dominguez-Gutierrez F.J. and Bedoya F. 2018 *Matter Radiat. Extrem.* **3** 165–87
[7] Goriaev A., Wauters T., Brakel R., Brezinsek S., Dinklage A., Fellinger J., Grote H., Moseev D., Sereda S. and Volzke O. 2020 *Phys. Scr.* **T171** 014063
[8] Vuoriheimo T., Hakola A., Likonen J., Brezinsek S., Dittmar T., Mayer M., Prakash Dhard C., Naujoks D. and Tuomisto F. 2021 *Phys. Scr.* **96** 124023
[9] Skinner C.H., Bedoya F., Scotti F., Allain J.P., Blanchard W., Cai D., Jaworski M. and Koel B.E. 2017 *Nucl. Mater. Energy* **12** 744–8
[10] Abe S. *et al* 2025 *Nucl. Mater. Energy* **42** 101855
[11] Afonin K. *et al* 2023 *Nucl. Fusion* **63** 126057
[12] Sereda S. *et al* 2020 *Nucl. Fusion* **60** 086007
[13] Dhard C.P. *et al* 2021 *Phys. Scr.* **96** 124059
[14] Mayer M. *et al* 2022 *Nucl. Fusion* **62** 126049
[15] Allen S.L. *et al* 2005 *J. Nucl. Mater.* **337** 30–34
[16] Airila M.I. *et al* 2009 *Phys. Scr.* **T138** 014021
[17] Stangeby P.C. 2011 *J. Nucl. Mater.* **415** S278–S83
[18] Möller S. *et al* 2020 *Nucl. Mater. Energy* **25** 100805
[19] Ohya K. and Kirschner A. 2009 *Phys. Scr.* **T138** 014010
[20] Schmid K., Reinelt M. and Krieger K. 2011 *J. Nucl. Mater.* **415** S284–S8
[21] Schmid K. *et al* 2020 *Nucl. Mater. Energy* **25** 100821
[22] Kawan C. *et al* 2024 *Nucl. Mater. Energy* **39** 101675
[23] Bol'shakov A.A., Mao X., González J.J. and Russo R.E. 2016 *J. Anal. At. Spectrom.* **31** 119–34
[24] Oelmann J., Wüst E., Sergienko G. and Brezinsek S. 2021 *Phys. Scr.* **96** 124064
[25] van der Meiden H.J. *et al* 2021 *Nucl. Fusion* **61** 125001
[26] Zhao D. *et al* 2022 *Phys. Scr.* **97** 024005
[27] Maurya G.S., Marín-Roldán A., Veis P., Pathak A.K. and Sen P. 2020 *J. Nucl. Mater.* **541** 152417
[28] Guo L.-B. *et al* 2021 *Front. Phys.* **16** 22500
[29] Wu H.C., Wu D., Li C., Hu Z., Ding F., Hai R. and Ding H. 2024 *Nucl. Fusion* **64** 086015
[30] Huber A. *et al* 2011 *Phys. Scr.* **T145** 014028
[31] Hu Z. *et al* 2017 *Phys. Scr.* **T170** 014046
[32] Semerok A., L'hermite D., Weulersse J.-M., Lacour J.-L., Cheymol G., Kempenaars M., Bekris N. and Grisolia C. 2016 *Spectroc. Acta Pt. B* **123** 121–8
[33] Almaviva S. *et al* 2021 *Fusion Eng. Des.* **169** 112638
[34] Favre A. *et al* 2024 *Phys. Scr.* **99** 035609
[35] Maurya G.S., Jyotsana A., Kumar R., Kumar A. and Rai A.K. 2014 *J. Nucl. Mater.* **444** 23–29
[36] Gierse N., Schweer B., Huber A., Karger O., Philipps V., Samm U. and Sergienko G. 2011 *J. Nucl. Mater.* **415** S1195–S8
[37] Sun L.Y., Wu D., Li C., Wu J., Hong S.-H., Bang E., Hu Z., Ding F., Luo G. and Ding H. 2022 *Nucl. Mater. Energy* **31** 101174
[38] Wu H.C., Yi R.X., Houben A., Brezinsek S., Rasinski M., Li C., Sergienko G., Liang Y., Dittmar T. and Ding H. 2024 *Nucl. Mater. Energy* **41** 101812
[39] Wu H.C., Yi R.X., Brezinsek S., Houben A., Rasinski M., Ding R., Mayer M., Sergienko G., Dittmar T. and Ding H. 2025 *Nucl. Mater. Energy* **45** 102018
[40] Traparic I., Rankovic D., Stankov B.D., Savovic J., Kuzmanovic M. and Ivkovic M. 2024 *Spectroc. Acta Pt. B* **221** 107050
[41] Favre A. *et al* 2024 *J. Nucl. Mater.* **591** 154924
[42] Harilal S.S., Shaik A.K., Kautz E.J., Devaraj A., Casella A.M. and Senor D.J. 2024 *J. Anal. At. Spectrom.* **39** 699–703
[43] De Giacomo A. and Hermann J. 2017 *J. Phys. D* **50** 183002
[44] Gaft M., Nagli L., Gornushkin I. and Raichlin Y. 2020 *Spectroc. Acta Pt. B* **173** 105989
[45] Mayer M. 1998 SIMNRA, a simulation program for the analysis of NRA, RBS and ERDA *15th Int. Conf. on the Application of Accelerators in Research and Industry* (University of North Texas, American Institute of Physics) pp 541–4
[46] Wüst E., Dittmar T., Kawan C., Romazanov J. and Brezinsek S. 2022 *Nucl. Mater. Energy* **33** 101287
[47] Mayer M. *et al* 2024 *Nucl. Mater. Energy* **41** 101778